













# Scintillation Bandwidth Measurements from 23 Pulsars from the AO327 Survey

Sofia Sheikh<sup>1,2,3,16</sup> , Grayce C. Brown<sup>1,2</sup> , Jackson MacTaggart<sup>4</sup> , Thomas Nguyen<sup>5,6</sup> , William D. Fletcher<sup>6</sup>,  
Brenda L. Jones<sup>7</sup>, Emma Koller<sup>6</sup>, Veronica Petrus<sup>6</sup>, Katie F. Pighini<sup>6</sup>, Gray Rosario<sup>6</sup>, Vincent A. Smedile<sup>8</sup> , Adam T. Stone<sup>9</sup>,  
Shawn You<sup>6</sup>, Maura A. McLaughlin<sup>10</sup> , Jacob E. Turner<sup>11</sup> , Julia S. Deneva<sup>12</sup> , Michael T. Lam<sup>1,13,14</sup> , and  
Brent J. Shapiro-Albert<sup>10,15</sup> 

<sup>1</sup> SETI Institute, 339 North Bernardo Avenue Suite 200, Mountain View, CA 94043, USA

<sup>2</sup> Berkeley SETI Research Center, Berkeley, CA 94720, USA

<sup>3</sup> Penn State Extraterrestrial Intelligence Center, University Park, PA 16802, USA

<sup>4</sup> Department of Climate and Space Sciences and Engineering, University of Michigan, Ann Arbor, MI 48109, USA

<sup>5</sup> The Applied Research Laboratory, The Pennsylvania State University, State College, PA 16802, USA

<sup>6</sup> Penn State Pulsar Search Collaboratory, Department of Astronomy & Astrophysics, The Pennsylvania State University, 525 Davey Laboratory, University Park, PA 16802, USA

<sup>7</sup> Department of Physics and Astronomy, The University of Maine, Orono, ME 04469, USA

<sup>8</sup> Department of Astronomy, The Ohio State University, 140 West 18th Avenue, Columbus, OH 43210, USA

<sup>9</sup> Department of Astronomy and Astrophysics, Department of Geosciences, The Pennsylvania State University, 201 Old Main, University Park, PA 16802, USA

<sup>10</sup> Department of Physics and Astronomy and the Center for Gravitational Waves and Cosmology, West Virginia University, Morgantown, WV 26506-6315, USA

<sup>11</sup> Green Bank Observatory, P.O. Box 2, Green Bank, WV 24944, USA

<sup>12</sup> George Mason University, 4400 University Drive, Fairfax, VA 22030, USA

<sup>13</sup> School of Physics and Astronomy, Rochester Institute of Technology, Rochester, NY 14623, USA

<sup>14</sup> Laboratory for Multiwavelength Astrophysics, Rochester Institute of Technology, Rochester, NY 14623, USA

<sup>15</sup> Giant Army, 17th Ave, Seattle, WA 98122, USA

Received 2024 July 26; revised 2024 October 7; accepted 2024 October 11; published 2024 November 26

## Abstract

A pulsar’s scintillation bandwidth is inversely proportional to the scattering delay, making accurate measurements of scintillation bandwidth critical to characterize unmitigated delays in efforts to measure low-frequency gravitational waves with pulsar timing arrays. In this pilot work, we searched for a subset of known pulsars within ~97% of the data taken with the Puerto Rico Ultimate Pulsar Processing Instrument for the AO327 survey with the Arecibo telescope, attempting to measure the scintillation bandwidths in the data set by fitting to the 2D autocorrelation function of their dynamic spectra. We successfully measured 38 bandwidths from 23 pulsars (six without prior literature values), finding that: almost all of the measurements are larger than the predictions from NE2001 and YMW16 (two popular galactic models); NE2001 is more consistent with our measurements than YMW16; Gaussian fits to the bandwidth are more consistent with both electron density models than Lorentzian ones; and for the 17 pulsars with prior literature values, the measurements between various sources often vary by a few factors. The success of Gaussian fits may be due to the use of Gaussian fits to train models in previous work. The variance of literature values over time could relate to the scaling factor used to compare measurements, but also seems consistent with time-varying interstellar medium parameters. This work can be extended to the rest of AO327 to further investigate these trends, highlighting the continuing importance of large archival data sets for projects beyond their initial conception.

*Unified Astronomy Thesaurus concepts:* [Radio pulsars \(1353\)](#); [Pulsars \(1306\)](#); [Interstellar medium \(847\)](#); [Interstellar scintillation \(855\)](#); [Interstellar scattering \(854\)](#); [Observational astronomy \(1145\)](#); [Radio astronomy \(1338\)](#)

## 1. Introduction

Pulsars are stellar remnants, formed via supernova at the end of the life cycle of a sufficiently massive star. Due to conservation of angular momentum and magnetic flux, pulsars have extremely high rotational speeds (with some periods on the order of a millisecond; D. R. Lorimer 2008) and associated strong magnetic fields (M. Ruderman 1972). As a result of the electromagnetic field strength, energetic particles in the pulsar’s magnetosphere are accelerated, creating synchrotron radiation that is forced by the rotating fields to the poles of the pulsar and

emitted in jets (D. R. Lorimer 2008). Depending on the geometry of the system relative to Earth, these jets may periodically emit along Earth’s line-of-sight. We can detect these jets across the electromagnetic spectrum, most commonly as remarkably regular bursts of dispersed emission in the broadband radio regime; this periodic emission led to the discovery of pulsars by A. Hewish et al. (1968).

Inhomogeneities in the ionized interstellar medium (ISM) can cause scattering in the radiation from a broadband radio source, especially one that is compact in spatial extent such as a pulsar, as the radiation propagates through the ISM. Scattering causes the radiation to constructively and destructively interfere, producing periodic variations of varying bandwidth and timescale in the radiation’s intensity as seen by some distant observer. This effect is called scintillation, and the relative motions of the observer, the pulsar, and the components of the ISM itself (B. J. Rickett 1990) will cause

<sup>16</sup> Corresponding author.



changes in other measured parameters, such as dispersion measures (DMs) and fluxes, over time. Diffractive interstellar scintillation (DISS) is produced over small spatial scales and is observable on minute to hour timescales at  $\sim$ GHz frequencies (e.g., Z. Wu et al. 2022), while refractive interstellar scintillation (RISS) is caused by larger spatial scales and is observable over weeks to months timescales at similar frequencies (e.g., B. J. Rickett & A. G. Lyne 1990).<sup>17</sup>

The effects of scintillation can be seen in the dynamic spectrum of an observation of a pulsar at radio wavelengths: interference maxima, or “scintles,” will appear as bright peaks in the plot of a pulsar’s pulse intensity over frequency and time. The characteristic widths in the scintles’ appearance in time and frequency can be parameterized by the “scintillation timescale”  $\Delta t_D$  and “scintillation bandwidth”  $\Delta \nu_D$  by measuring the half-width at half-maximum (HWHM) in the 2D autocorrelation function (2D ACF) of the dynamic spectrum. Density fluctuations and turbulence of the ISM along the line of sight affect both quantities (e.g., N. Wang et al. 2005). Additionally, observations that are long enough to derive both the scintillation bandwidth and timescale from DISS can provide the 2D power spectrum to the dynamic spectrum, revealing “scintillation arcs” (D. R. Stinebring et al. 2001; M. A. Walker et al. 2004; J. M. Cordes et al. 2006) whose properties constrain the distance to a scattering screen and the transverse motion of the pulsar.

The scattering delay  $\tau_s$  is the broadening timescale, which causes a mean-shift delay (e.g., D. A. Hemberger & D. R. Stinebring 2008).  $\Delta \nu_D$  relates to  $\tau_s$  by:

$$2\pi\tau_s\Delta\nu_D = C \quad (1)$$

where  $C$  is a factor  $\sim 1$ – $2$  that depends on the geometry and electron density wavenumber spectrum. If a thin screen is assumed,  $C=1$  for a medium that follows a square-law structure function, and  $C=0.96$  for a medium that follows a Kolmogorov-type structure function (J. M. Cordes & B. J. Rickett 1998).

These observational signatures can be used to derive the properties of the ISM on the line of sight between Earth and a scintillating pulsar (e.g., N. Wang et al. 2005), calculate precise orbits of binary pulsars (e.g., D. J. Reardon et al. 2020), and, with the relation to scattering delay defined above, generate timing corrections for gravitational-wave characterization using pulsar timing arrays (e.g., Y. Liu et al. 2022), such as those observed by NANOGrav (G. Agazie et al. 2023; Z. Arzoumanian et al. 2023), the EPTA (S. Chen et al. 2021), the PPTA (D. J. Reardon et al. 2021), and the InPTA (P. Tarafdar et al. 2022).

Understanding the distribution of free electrons in the galaxy via modeling the structure of the ionized ISM is critical for Galactic composition work, and for understanding the distance to radio sources such as pulsars and fast radio bursts (D. C. Price et al. 2021). One widely used model, NE2001 (J. M. Cordes & T. J. W. Lazio 2002), combined scintillation bandwidth measurements from many pulsars across the celestial sphere with independent distance constraints from e.g., absorption lines in the local hot ISM. More recently, M. A. Krishnakumar et al. (2015) developed an empirical DM–scintillation bandwidth relationship that J. M. Yao et al. (2017) combined with almost 200 pulsar distances and DMs, as well

as H II regions and other observational calibrators, to create the YMW16 model.

However, by using astrometry to provide independent distance measurements for several dozen pulsars, A. T. Deller et al. (2019) found that NE2001 and YMW16 still have significant flaws, especially at high Galactic latitudes<sup>18</sup>: some pulsars have significant errors in their DM-derived distances, and both models tend to underestimate the distance to pulsars. Obtaining scintillation bandwidths, and therefore more constraints on electron density and ISM structure, can help improve the next generation of electron density models.

One way to do this is by leveraging existing data sets, such as the archival 327 MHz drift-scan survey (AO327) from the sadly collapsed 305 m Arecibo telescope (J. S. Deneva et al. 2013). However, when using archival data, one must navigate design choices made for other purposes—in this case, pulsar discovery. Using drift rate data for scintillation work leads to an obvious drawback: the short amount of time that each pulsar is in the beam is much shorter than the scintillation timescale, even for DISS. Therefore, we can only use this data set to extract  $\Delta \nu_D$ , but cannot place constraints on  $\Delta t_D$ .  $\Delta \nu_D$ , however, is the parameter that can be converted to scattering delay and can be used to help evaluate electron density fluctuations along different sightlines of the galaxy in comparison with models.

In this paper, we describe a search for known pulsars with measurable scintillation bandwidths in AO327, analyze their archival observations, and provide bandwidths and comparisons to electron density model predictions. In Section 2, we describe the AO327 survey and the source selection. In Section 3, we describe the analysis pipeline, including radio frequency interference (RFI) removal, downsampling, and model fitting. In Section 4, we discuss each measurement at a per-pulsar level, including a comparison to predictions from existing models, and a discussion of results at a population level. We conclude in Section 5.

## 2. Observations and Data

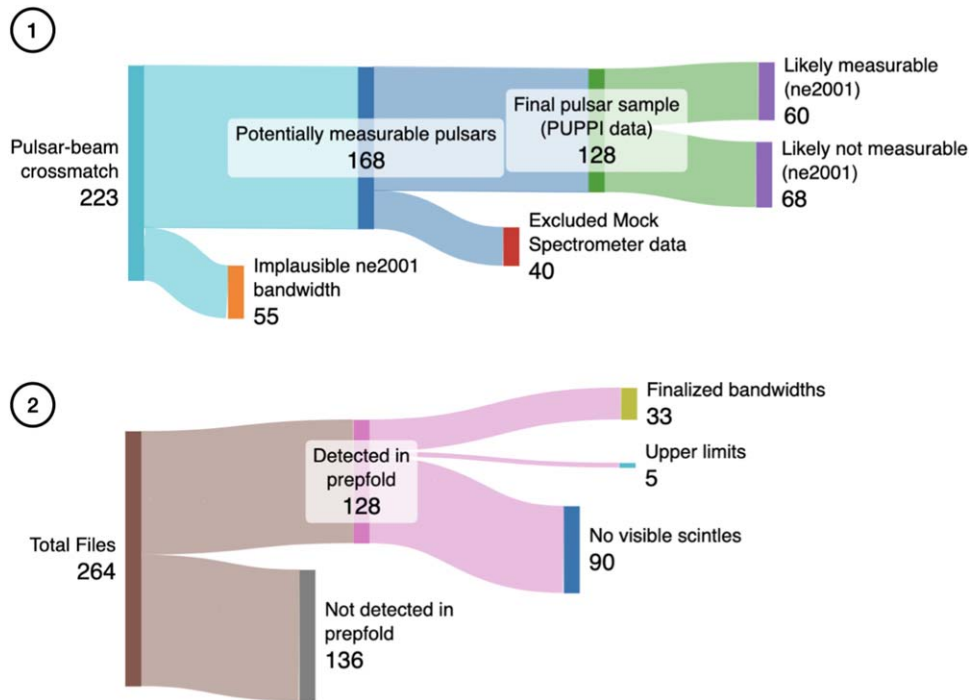
### 2.1. AO327

AO327 is a drift-scan pulsar survey that was conducted with the 305 m Arecibo telescope at a central frequency of 327 MHz. Details of the campaign design are provided in J. S. Deneva et al. (2013) and recent pulsar detections are covered in J. S. Deneva et al. (2024). We summarize the important parameters here. When taking data in a “drift-scan” mode, the telescope remains fixed on a particular azimuth and altitude while the sky rotates overhead: for Arecibo, this led to an effective integration time of 60 s for a celestial object to pass through the primary beam, leading to 60 s “strips” of coverage in R.A. at the pointing decl. Beginning in 2010, AO327 took data during downtime or unassigned time on Arecibo (J. S. Deneva et al. 2016), gathering thousands of hours of data with the Mock Spectrometer, from which nearly a hundred pulsars and rotating radio transients (RRATs) have been discovered (J. S. Deneva et al. 2013, 2016; J. G. Martinez et al. 2019).

The Puerto Rico Ultimate Pulsar Processing Instrument (PUPPI) backend, installed in 2012, allowed for the recording of 69 MHz of dual-linear polarization bandwidth, centered at 327 MHz; this bandwidth was channelized into 2816 frequency

<sup>17</sup> DISS and RISS are two regimes in a continuous parameter space, and some science cases do benefit from breaking down the dichotomy by exploring edge cases or modeling in a purely refractive way (e.g., D. L. Jow et al. 2023).

<sup>18</sup> Work is being done on YMW16 to mitigate these flaws, e.g., S. K. Ocker et al. (2020).



**Figure 1.** Two Sankey diagrams generated with Sankeymatic (S. Bogart 2024) illustrating (1) the path of pulsars from initial identification in the data set to selection for analysis in Section 3 and (2) the result of each PUPPI PSRFITS file from each of those pulsars, leading to the 38 measurements we report in Section 4. In subfigure (1), there are two separate NE2001 filtering steps, indicating the original incomplete filtering described in Section 2.2.

channels and sampled at  $81.92 \mu\text{s}$  (J. S. Deneva et al. 2013). The receiver temperature for the instrument was 113 K, and the gain was  $11 \text{ K Jy}^{-1}$ . For reference, the Mock spectrometer had 0.336 MHz wide frequency channels; the PUPPI backend improved on this with a finer, 0.025 MHz channelization. When taken together, the benefits of the survey—the incredible sensitivity of the Arecibo telescope; the wide bandwidth, relatively low center frequency, and suitable frequency resolution of the PUPPI backend; and its huge volume of on-sky time and archival data—make it a fantastic instrument for measuring scintillation bandwidths. The archival data from AO327 are saved as PSRFITS files, with each individual PSRFITS file containing about 1 hr of data.

## 2.2. Data Selection

The data used in this work are a subset of the data collected for AO327. The observations span from MJD 56608 to 59065, and initially included observations taken with both the PUPPI and Mock spectrometers.

To identify pulsars from which we could measure scintillation in frequency, we took each pointing in the available data set and defined a generous pointing radius of  $15'$ , equivalent to twice the full-width at half-maximum (FWHM) of the beam at 327 MHz. We cross-matched these pointings with a list of 223 pulsars that were identified in or discovered by AO327 at the beginning of this work in 2019.

We took those 223 objects and calculated their expected scintillation bandwidths with NE2001, with error bars corresponding to bandwidth calculated at  $\pm 20\%$  of the fiducial distance;<sup>19</sup> 20% represents the distance uncertainty given in J. M. Cordes & T. J. W. Lazio (2003) from, e.g., unmodeled clumps in the ISM. We determined that the narrowest scintles

we could resolve with either of the spectrometers on the 327 MHz receiver would be approximately five times their frequency resolution  $\Delta\nu$ ; similarly, we estimated that the largest scintle size that we could resolve is approximately half of the bandwidth. We then compared the NE2001 estimates to these values—if any value within the error bars of the NE2001 estimate fell within the measurable scintle bounds described above, we deemed the pulsar potentially measurable. This filtered our sample to 60 objects. However, 108 objects were additionally, incorrectly, added to the sample due to an error in the input center frequency when calculating the predicted scintillation bandwidths. These 108 objects had true predicted bandwidths that were likely narrower than what we could measure with the AO327 archival data. However, we took them through the same pipeline anyway, giving us 168 pulsars total.

The majority of these pulsars, 128 of the 168, were observed with the more modern PUPPI spectrometer on Arecibo. The Mock spectrometer was used to take a significant fraction of the early AO327 data but given its limited presence in our sample and its less-optimal parameters for scintillation measurement (i.e., wider channels), we decided to only use PUPPI data in this work for consistency. We searched through  $\sim 97\%$  of the total PUPPI data taken for AO327, with the remaining 3% representing data taken in the few months before Arecibo’s collapse.

Some of these pulsars had multiple observations in different strips, observed on different days. We include 264 individual 4 bit PSRFITS files, corresponding to scans within a  $15'$  radius of the 128 sample pulsars. Overall, this sample has relatively uniform coverage in R.A. and declinations visible to Arecibo, which is ideal for comparison with electron density models. The full selection path for both pulsars and files is shown in Figure 1.

For comparison, recent work in J. S. Deneva et al. (2024) found 206 pulsars within the AO327 PUPPI data, using a

<sup>19</sup> pygedm (D. C. Price et al. 2021) was used as the NE2001 interface.

pointing radius of  $7.5$  ( $1/2$  of what we assumed above). Meanwhile, 40% of pulsars in the J. S. Deneva et al. (2024) list are included in this work; our sample was determined before the full PUPPI data set had been searched for pulsar emission, leading to the discrepancy.

Interestingly, this pilot study serendipitously gives us insight into how the different choices of beamwidth affect the recovered pulsar sample. Though the recovery fraction (number of predicted pulsars detected in folded data, as described in Section 3.1) is lower for our pulsars that are outside the beam’s FWHM, we still manage to detect an additional 27 pulsars that would not be considered if using the  $7.5$  FWHM as the pointing boundary. In future work with the AO327 sample, we recommend cross-matching pulsar catalogs with this larger radius if vetting time allows in order to recover and characterize pulsars that are entering the beam through the sidelobes.<sup>20</sup>

### 3. Data Analysis

#### 3.1. Identifying Detections with *prepfold*

To identify whether a pulsar was detected in an observation, we folded the data using the *prepfold* function from the Pulsar Exploration and Search Toolkit (PRESTO), a large suite of pulsar search programs and software (S. Ransom 2011). The *prepfold* program dedisperses and folds pulsar data to create output summary plots within which true pulsar detections are quite obvious compared to RFI. We folded our data according to parameters from the ATNF<sup>21</sup> Pulsar Catalogue (R. N. Manchester et al. 2005); specifically, period and DM. Since we knew that each of these particular pulsars should be in the data based on the filtering from Section 2.2, we inputted the known parameters into *prepfold* instead of having the function search through a grid of DMs and periods. This method searches a small part of parameter space around the input period and DM, allowing for accurate folding even without a full timing ephemeris. It should be noted that this method will not always work for binary pulsars, which constituted 10 of the original 223 objects; the only one of these which had visible scintles was B0820+02, which is discussed in Section 4.5.

The time-phase plot of the *prepfold* summary plot is a good diagnostic of whether or not a pulsar was detected. If there is a pulsar in the data, it will appear in the time-phase subplot as two dark, vertical lines. Since the length of the observation was much greater than the amount of time the pulsar spent in the beam, we cropped the observation to the times where the pulsar was visibly in the beam. After creating and inspecting the 264 *prepfold* plots, we removed 136 PSRFITS files from our sample where the pulsar was not detected, leaving 128 files with sufficient pulsar signal to analyze in the next step. The pulsars that we did not detect were generally the ones furthest from the beam (between 1 and 2 times the FWHM) and the intermittent pulsars (i.e., pulsars which do not consistently emit, such as RRATs or nulling pulsars), as expected.

<sup>20</sup> Arcing RFI from geostationary satellites has been observed in Arecibo data, even when the satellites were in the extended sidelobes a few degrees away from the main beam (D. C. Ferguson et al. 2022).

<sup>21</sup> <http://www.atnf.csiro.au/research/pulsar/psrcat>

#### 3.2. Folding

Once we identified the time range containing a pulsar, we created folded output files from the PSRFITS files described in Section 2.1 using the *fold\_psrfits* function from *psrfits\_utils*, a utility library for working with PSRFITS pulsar files.<sup>22</sup> We used the same ATNF values from the *prepfold* commands above to create three output folded PSRFITS files for each pulsar observation, with time integrations of 5, 10, and 20 s. Generally, the 20 s integrations had the highest signal-to-noise ratio (SNR) and were used in the following steps, but for some observations it was advantageous to use the shorter integrations to mitigate RFI and/or provide sufficient time bins for *PyPulse* to successfully produce a dynamic spectrum (see Section 3.4). Each output file was also reduced to 64 phase bins to increase SNR at this step.

#### 3.3. *pazi* and *Fscrunch*

We used the *pazi* tool from PSRCHIVE (A. W. Hotan et al. 2004) to remove RFI from the folded data by zapping frequency channels and time bins with significant interference. The most common RFI signal that we observed was a bright, narrowband emitter near 312 MHz which, if not excised, would entirely override the *PyPulse* pulse identification within the dynamic spectrum in a later step. After using *pazi*, we reduced the number of frequency bins by “fscrunching,” or summing adjacent frequency bins to increase SNR using the *pam* utility. In this process, we were cautious not to overscrunch the data beyond either the limit of five data points across from NE2001 in Section 2.2, nor to overscrunch empirically based on visible scintles in the dynamic spectrum.

#### 3.4. *PyPulse*

We used the Python library *PyPulse* (M. Lam 2017) to create the dynamic spectra which were the basis of the scintillation bandwidth measurements. We initiated each cropped, RFI-cleaned, and frequency scrunched file into the *Archive* class within *PyPulse*. We also generated a pulse template, created by averaging the file in time, frequency, and polarization, and then smoothing the new profiles with the *psrsmooth* function of PSRCHIVE. *PyPulse* uses the data and the pulse template to generate a pulse-sensitive dynamic spectrum that integrates all intensity across the pulse for each “pixel” of the dynamic spectrum’s time-frequency grid. At this point, if there were any additional time bins without pulsar signal (e.g., fading on the edges due to the pulsar entering or leaving the beam), they were cropped out of the dynamic spectrum to improve SNR for the following steps.

#### 3.5. 2D ACF

We then performed a 2D ACF on the dynamic spectra using the *acf2d* function in the *PyPulse* package. Generally, when the ACF method has been used to measure scintillation bandwidth in prior studies (e.g., N. Wang et al. 2005), both axes (time and frequency) of the data are lagged and then used for measurement of  $\Delta\nu_D$  and  $\Delta t_D$ . As mentioned in Section 2, our short observation times do not provide any useful measurements across the time axis of the 2D ACF. Therefore, we take the sum across the time lag axis to produce a “slice” of

<sup>22</sup> Written by P. Demorest and S. Ransom and available at [https://github.com/demorest/psrfits\\_utils](https://github.com/demorest/psrfits_utils).

scaled flux density versus frequency lag, which will have a morphology with a central peak of some measurable width. We opt to use the sum across the time lag axis in this work because we are dealing with short observation times; the sum across the time lag axis recoups some SNR and does not suffer here from additional artifacts that would occur with longer observation times. We acknowledge that this method is not without its own minor drawbacks (e.g., including noise in the outskirts, summing features of differing widths), but do not find them significant enough to affect the results of the work.

### 3.6. Fitting for Scintillation Bandwidth

Even after these multiple phases of data reduction, there are a few frequency-dependent effects that may still be present in the 2D ACF, e.g., rolloff of intensity at the edges of the bandpass. To ensure that we are measuring purely pulsar scintillation, we crop the data in the frequency-lag axis to contain only the smallest coherent structure in the peak with at least five data points, so as to avoid fitting to only the direct current (DC) spike at lag = 0. In cases where the peak is narrower than five points across the ACF slice (<0.084 MHz), we do not fit a model and instead report an upper limit, indicating that the actual bandwidth is narrower than we can measure. We fit this structure with both a Gaussian model (used more commonly in the literature) and a Lorentzian model (a better mathematical fit to the assumed ISM structure) using the `curve_fit` function from `scipy.optimize` (P. Virtanen et al. 2020).

The Gaussian model is described by:

$$A \exp\left(\frac{-(x - \mu)^2}{2\sigma^2}\right) + y \quad (2)$$

where  $A$  determines the amplitude of the Gaussian,  $\mu$  determines its location along the frequency-lag axis,  $\sigma$  determines its width, and  $y$  determines its vertical offset from 0. We set  $\mu$  to 0 because the ACF is always guaranteed to be symmetric.

The Lorentzian model is described by:

$$A \left( \frac{w}{x^2 + w^2} \right) + y \quad (3)$$

where  $A$  determines the amplitude of the Lorentzian,  $w$  determines its width, and  $y$  determines its vertical offset from 0.

From the width parameters, we can convert to a  $\Delta\nu_D$  by taking the HWHM—equivalent to the width parameter for the Lorentzian and equal to  $\sqrt{2\ln 2}$  times the width parameter (standard deviation) for the Gaussian.

### 3.7. Calculating Errors in the Fit

We incorporated three sources of error, added in quadrature, which we report alongside the final scintillation bandwidth measurements: finite scintle error (FSE), fit error, and channel width uncertainty.

FSE accounts for the fact that there can only be a finite amount of scintles observed in a limited bandwidth. This effect is stronger when the scintles are proportionally larger in the bandpass, due to there being fewer scintles. We calculate FSE using the method from J. Cordes (1986):

$$\text{FSE}_{\Delta\nu, \text{Gauss}} = \frac{\Delta\nu_D}{2\ln(2)N_{\text{scint}}} \quad (4)$$

where  $N_{\text{scint}}$  is the number of scintles in the observation.  $N_{\text{scint}}$  is normally defined as the number of scintles in frequency multiplied by the number of scintles in time— $N_\nu N_\tau$ —but here our observation time is much shorter than  $\Delta\nu_D$  and thus  $N_\tau = 1$ . Thus, using the formulation from J. Cordes & R. Shannon (2010):

$$N_{\text{scint}} = N_\nu = 1 + \frac{\eta_\nu B}{\Delta\nu_D} \quad (5)$$

where  $\eta_\nu$  is a filling factor that we set to 0.2 (as in J. Cordes & R. Shannon 2010; J. E. Turner et al. 2021) and  $B$  is the bandwidth of the observation. Equation (5) can then be inserted into Equation (4) to obtain the FSE.

We also included the fit error on the width parameters ( $\sqrt{2\ln 2}$  times the *square root of the variance*  $\sigma$  for the Gaussian fit, the *square root of the variance*  $w$  directly for the Lorentzian fit) from `curve_fit`. To account for the uncertainty in particularly narrow scintles, we also added an additional error term equal to the width of half of a frequency channel after frequency scrunching.

To visualize the entire analysis process in Section 3, we summarize four major steps using the output plots from our analysis pipeline in Figure 2.

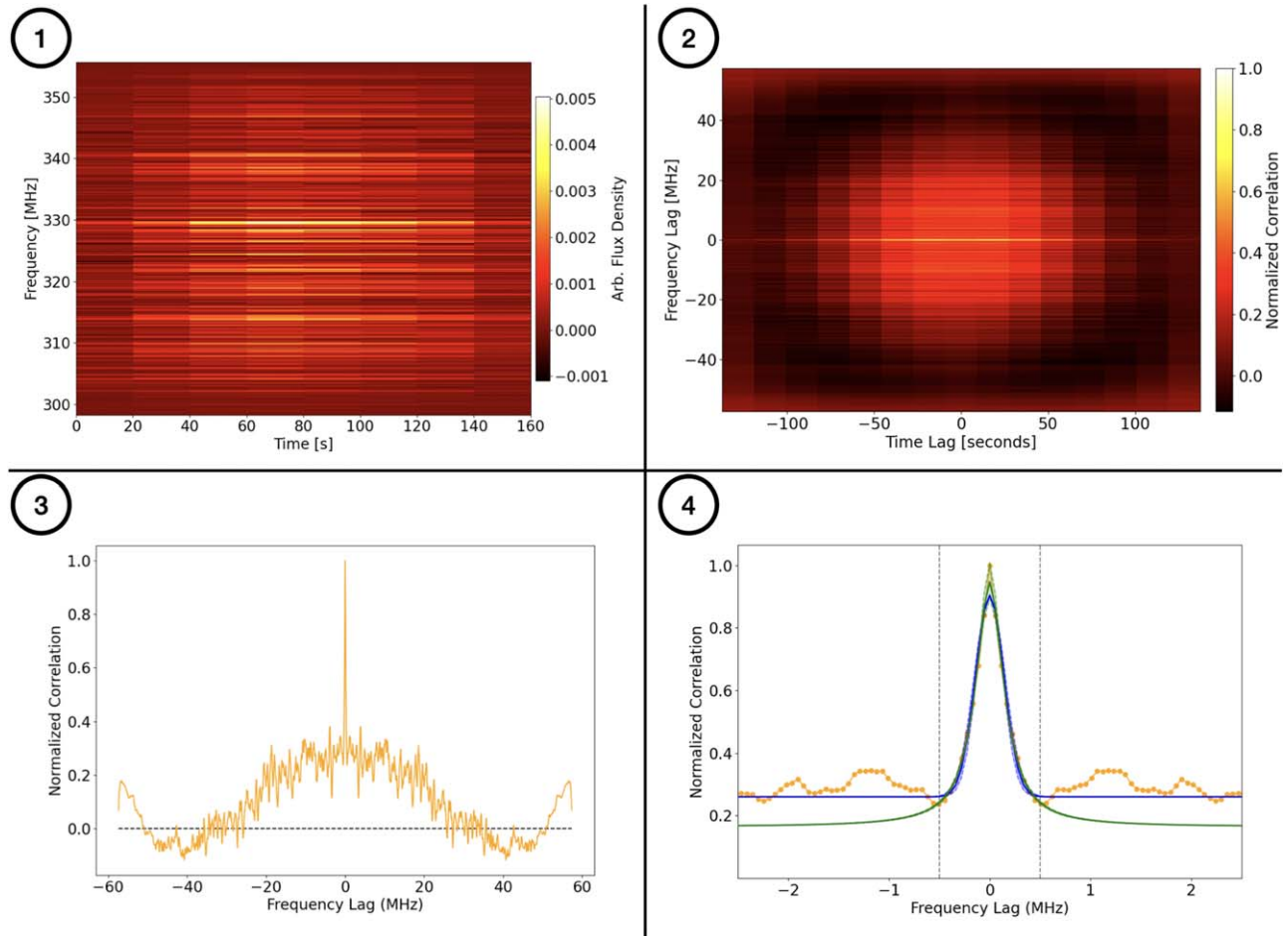
## 4. Results

Using the analysis procedure from Section 3, we measured 38 scintillation bandwidths,  $\Delta\nu_D$ , from 23 unique pulsars. In Table 1, we report the  $\Delta\nu_D$  values for both Gaussian and Lorentzian fits with their associated error (reported with  $\delta$ ), compare these values to predictions from NE2001 and YMW16,<sup>23</sup> and provide the same information converted to scattering time,  $\tau_s$ , using the relation defined in Equation (1).

We also quantitatively compare the  $\Delta\nu_D$  measurements for each pulsar with their previously measured values in the literature as summarized in Table 2. For each pulsar and each reference in Table 2, we provide the equivalent scintillation bandwidth at 327 MHz  $\nu_{D,327}$  (MHz) and the equivalent scattering timescale  $\tau_{s,327}$  ( $\mu\text{s}$ ), along with a reference key. For references that originally reported a scattering timescale, we convert from scattering measurements to bandwidth equivalents using Equation (1), where we use  $C = 1.53$  to align with J. H. Taylor et al. (1993) and  $C = 0.96$  in all other cases to be consistent with a Kolmogorov thin-screen model. For all measurements, after converting from scattering timescale to bandwidth as necessary, we scale from the original measurement frequency to 327 MHz using a Kolmogorov scaling index of  $\alpha = 4.4$  as in B. J. Rickett (1977). It should be noted that scaling indices have been found to vary significantly from 4.4, generally tending smaller (e.g., L. Levin et al. 2016), because that value is only true for an ideal screen where inner scale and refractive effects are ignored (J. E. Turner et al. 2021).

In Table 2, rows with “This Work” have been averaged from all of this work’s observations of each pulsar using the result from the Gaussian fit (as justified in Section 4.8). Errors are not included in the values from Table 2 because different works

<sup>23</sup> Note that YMW16 does not directly make predictions for scintillation bandwidth based on structures in the ISM, but uses the empirical relationship derived by M. A. Krishnakumar et al. (2015), which is what is used in this work.



**Figure 2.** An example of the analysis pipeline described throughout Section 3 for a scan of pulsar B2315+21. Subplot (1): The dynamic spectrum after loading into PyPulse with a pulse template. Time is shown on the horizontal axis and frequency on the vertical axis. The pulsar fades in as it enters the drift-scan beam and then fades out as it leaves the beam a few minutes later. Scintillation is visible in the horizontal striping across the pulsar’s signal from top-to-bottom. Subplot (2): The 2D autocorrelation function (2D ACF) of the dynamic spectrum, showing the correlation of the signal with a delayed copy of itself as a function of lag (delay) in time and frequency. The correlation coefficient is a measure of similarity between the signal and its copy, with the central peak normalized to unity. The frequency lag is shown on the vertical axis and the time lag is shown on the horizontal axis. The horizontal extent (in time lag) only indicates the time that the pulsar was in the beam, not the scintillation timescale, and is thus unimportant for this study. The width of the narrowest horizontal stripe in the 2D ACF is indicative of the scintillation bandwidth corresponding to the stripes in Subplot (1). Subplot (3): The 2D ACF “slice,” created by summing the 2D ACF in Subplot (2) along the time axis. The narrowest peak in this image can be fitted with a Gaussian or Lorentzian to measure the scintillation bandwidth. For some faint pulsars, the bounds of the fit will be determined by crossing points where the correlation coefficient becomes negative (dashed line). Subplot (4): The 2D ACF slice from Subplot (3), but zoomed in to the middle few MHz and overplotted with both a best-fit Lorentzian (green) and a best-fit Gaussian (blue) to the points between the vertical gray dashed lines, using a least squares fitting method. These are the measurements reported in Table 1.

have incompatible standards of presenting and calculating errors.

Finally, to evaluate trends in model over- or underestimation for each pulsar’s scintillation bandwidth, we quantified the amount of difference between the prediction and the measurement using a simple difference factor (DF) calculated with:

$$\text{Difference Factor} = \frac{\Delta\nu_{D,\text{measured}} - \Delta\nu_{D,\text{predicted}}}{\Delta\nu_{D,\text{predicted}}}. \quad (6)$$

Note that we evaluate consistency in the following sections using  $1\sigma$  errors. We comment upon a few interesting subpopulations and measurements in the subsections below.

#### 4.1. Pulsars with No Literature Values

We measured the scintillation bandwidths for the following pulsars for the first time because there were no reported measurements in the literature in the form of either scintillation bandwidths or scattering timescales. We obtained a single

measurement each for J2227+3038, J2253+1516, J0137+1654, J1313+0931, and J1612+2008, all of which were larger than the model predictions. In our data set, we obtained two measurements of J2215+1538—one upper limit consistent with the narrow estimate from both models, and the other measured value larger than both models’ predictions.

#### 4.2. Pulsars with Negative Difference Factor

Most pulsars that we measured were either consistent with or had larger scintillation bandwidth values than the model predictions, as will be discussed in Section 4.8. The following pulsars, in contrast, have measured scintillation bandwidth values which are smaller than some of the model predictions.

We measured one observation for the scintillation bandwidth for B0950+08. The model predictions were quite different for this pulsar—101 MHz for NE2001 versus 4 MHz for YMW16—and the measured value fell between these bounds. We find

**Table 1**  
The 38 Scintillation Bandwidth Measurements  $\Delta\nu_D$  Reported in this Study, and Their Equivalent Scattering Timescales  $\tau_s$

Pulsar	MJD	$\Delta\nu_{D,Lor}$ (MHz)	$\Delta\nu_{D,Gauss}$ (MHz)	$\Delta\nu_{D,NE2001}$ (MHz)	$\Delta\nu_{D,YMW16}$ (MHz)	$\tau_{s,Lor}$ ( $\mu$ s)	$\tau_{s,Gauss}$ ( $\mu$ s)	$\tau_{s,NE2001}$ ( $\mu$ s)	$\tau_{s,YMW16}$ ( $\mu$ s)
B0301+19	55543	<0.084	<0.084	0.054	0.070	>1.82	>1.82	2.9	2.3
B0301+19	58237	<0.084	<0.084	0.054	0.070	>1.82	>1.82	2.9	2.3
B0820+02	58225	0.09(1)	0.10(1)	0.055	0.020	1.6(2)	1.4(2)	2.9	8.0
B0820+02	58977	0.07(1)	0.07(1)	0.055	0.020	2.1(4)	2.1(4)	2.9	8.0
B0823+26	57029	0.21(2)	0.21(2)	0.077	0.037	0.73(8)	0.74(8)	2.1	4.3
B0834+06	58980	0.4(1)	0.4(1)	0.21	0.12	0.4(1)	0.4(1)	0.76	1.3
B0919+06	58915	0.15(2)	0.15(2)	0.018	0.013	1.0(1)	1.0(1)	8.8	13
B0919+06	58923	0.13(2)	0.10(1)	0.018	0.013	1.2(2)	1.5(2)	8.8	13
B0919+06	58980	0.12(1)	0.13(2)	0.018	0.013	1.2(2)	1.2(1)	8.8	13
B0950+08	58848	31(18)	20(11)	101	4.0	0.005(3)	0.007(4)	0.0016	0.040
B1237+25	58287	10(5)	9(4)	0.21	0.29	0.015(7)	0.018(9)	0.77	0.56
B1237+25	55556	4(2)	4(1)	0.21	0.29	0.04(1)	0.04(1)	0.77	0.56
B1530+27	58234	0.49(6)	0.40(5)	0.34	0.085	0.31(4)	0.38(5)	0.47	1.9
B1929+10	58496	0.61(9)	0.56(8)	5.5	3.4	0.25(4)	0.27(4)	0.029	0.047
B1929+10	58673	2.0(5)	2.0(5)	5.5	3.4	0.07(2)	0.08(2)	0.029	0.047
B1929+10	58726	1.3(2)	1.0(2)	5.5	3.4	0.12(2)	0.15(3)	0.029	0.047
B1952+29	57966	0.8(4)	0.6(2)	0.21	0.42	0.2(1)	0.28(8)	0.75	0.38
B2016+28	58055	0.13(2)	0.11(1)	0.038	0.093	1.1(4)	1.4(2)	4.2	1.7
B2016+28	58058	0.14(2)	0.15(2)	0.038	0.093	1.1(1)	1.0(1)	4.2	1.7
B2020+28	58055	0.27(3)	0.22(2)	0.056	0.018	0.57(6)	0.68(7)	2.9	9.0
B2020+28	58056	0.28(6)	0.27(6)	0.056	0.018	0.5(1)	0.6(1)	2.9	9.0
B2020+28	58057	0.26(3)	0.26(3)	0.056	0.018	0.59(7)	0.58(6)	2.9	9.0
B2110+27	56608	0.05(1)	0.05(1)	0.066	0.017	3.0(7)	2.8(7)	2.4	9.6
B2110+27	57004	0.07(1)	0.07(1)	0.066	0.017	2.1(4)	2.3(4)	2.4	9.6
B2110+27	57145	0.06(1)	0.07(1)	0.066	0.017	2.6(5)	2.2(4)	2.4	9.6
B2110+27	58331	0.06(1)	0.06(1)	0.066	0.017	2.7(6)	2.6(6)	2.4	9.6
B2315+21	55546	0.17(3)	0.17(3)	0.090	0.030	0.9(2)	0.9(2)	1.8	5.3
J0051+0423	56795	0.47(6)	0.41(5)	0.078	0.099	0.32(4)	0.38(5)	2.1	1.6
J0051+0423	56868	0.35(5)	0.33(4)	0.078	0.099	0.44(6)	0.47(6)	2.1	1.6
J0137+1654	58423	0.03(1)	0.02(1)	0.018	0.014	6(3)	7(3)	8.7	12
J1313+0931	57037	0.35(6)	0.31(6)	0.088	0.15	0.44(8)	0.49(9)	1.8	1.1
J1612+2008	58251	0.32(7)	0.25(6)	0.029	0.037	0.5(1)	0.6(2)	5.4	4.3
J1652+2651	57159	<0.084	<0.084	0.0053	0.0030	>1.82	>1.82	30	53
J1758+3030	57753	<0.084	<0.084	0.012	0.0053	>1.82	>1.82	13	30
J2215+1538	56759	0.04(1)	0.04(1)	0.017	0.0099	3(1)	4(1)	9.2	16
J2215+1538	56848	<0.084	<0.084	0.017	0.0099	>1.82	>1.82	9.2	16
J2227+3038	58264	0.19(2)	0.21(2)	0.016	0.0065	0.80(9)	0.74(8)	9.9	24
J2253+1516	58638	0.03(1)	0.03(1)	0.016	0.010	5(2)	5(2)	10	16

that our measurement is inconsistent with that of previous literature (e.g., J. H. Taylor et al. 1993; A. D. Kuz'min et al. 2007) but is consistent with others (e.g., N. D. R. Bhat et al. 1998; V. V. Zakharenko et al. 2013), including, notably, a wide-bandwidth investigation of B0950+08 over four distinct frequency ranges (T. V. Smirnova & V. I. Shishov 2008).

We measured four bandwidth values for B2110+27, which were generally consistent with each other and NE2001 and a few times larger than YMW16. The mean for both the Lorentzian and Gaussian measurements was  $0.06 \pm 0.01$  MHz. This is consistent with some prior reports in the literature (J. H. Taylor et al. 1993; A. D. Kuz'min et al. 2007), but not V. V. Zakharenko et al. (2013).

We made three measurements of B1929+10, two of which were consistent with each other within  $1\sigma$  error. All three measurements were lower than the values predicted by NE2001 and YMW16. The measurement in J. H. Taylor et al. (1993) is consistent with our lowest measurement, while the measurement from F. G. Smith & N. C. Wright (1985) falls within the range of our three measurements. The mean for the Lorentzian measurement was  $1.3 \pm 0.6$  MHz and for the Gaussian measurement was  $1.2 \pm 0.6$  MHz.

#### 4.3. Particularly Narrow Pulsars (Upper Limit Only)

Pulsars in this category have scintillation bandwidth measurements which are upper limits, indicating that the actual bandwidth is narrower than we can measure ( $<0.084$  MHz, or five points across the ACF slice described in Section 3.6). We set an upper limit on two observations for the scintillation bandwidth for B0301+19, which is consistent with both NE2001 and YMW16, as well as with A. D. Kuz'min et al. (2007) and J. H. Taylor et al. (1993) but not with F. G. Smith & N. C. Wright (1985), who found a larger value. We set an upper limit on one observation each for the scintillation bandwidths for J1652+2651 and J1758+3030 which were consistent with both NE2001 and YMW16, as well as A. D. Kuz'min et al. (2007), which is the only measured value in the literature. J2215+1538 has one upper limit measurement and is discussed in full in Section 4.1.

#### 4.4. Unexpected Measurements based on Sample Selection

We did not expect to be able to measure bandwidths for these pulsars because their scintillation bandwidths were predicted to be too small for us to resolve at the observing

**Table 2**  
A Summary of all Literature Values for the 23 Pulsars Included in this Study

Pulsar	$\nu_{\text{scint}, 327}$ (MHz, Conv.)	$\tau_{\text{sc}, 327}$ ( $\mu\text{s}$ , Conv.)	References	Pulsar	$\nu_{\text{scint}, 327}$ (MHz, Conv.)	$\tau_{\text{sc}, 327}$ ( $\mu\text{s}$ , Conv.)	References
B0301+19	0.0455	3.36	KLL	B1237+25	0.89	0.17	Z
	0.0387	3.94	TML		1.5	0.10	S&W
	0.23	0.67	S&W		0.334	0.457	C&L 2003
	0.062	2.5	C&L 2003		6.1	0.025	This Work
B0820+02	<0.084	>1.8	This Work	B1530+27	0.0223	6.85	KLL
	0.0387	3.94	TML		0.173	0.883	TML
	1.5	0.10	S&W		0.197	0.776	BGR
	0.062	2.5	C&L 2003		0.63	0.24	Z
	0.013	12	This Work		0.278	0.550	C&L 2003
B0823+26	0.134	1.14	KLL	B1929+10	0.40	0.38	This Work
	0.0435	3.52	TML		0.628	0.243	TML
	0.057	2.7	DLK		0.83	0.18	S&W
	0.293	0.521	BGR		1.01	0.151	C&L 2003
	0.34	0.45	Z		1.2	0.13	This Work
	0.19	0.81	S&W		B1952+29	0.165	0.925
0.070	2.2	C&L 2003	0.18	0.86		Z	
0.21	0.73	This Work	1.5	0.10		S&W	
0.122	1.25	TML	0.265	0.576		C&L 2003	
B0834+06	0.454	0.337	BGR	B2016+28	0.55	0.28	This Work
	0.21	0.73	Z		0.0154	9.91	KLL
	0.60	0.25	S&W		0.0287	5.32	TML
	0.197	0.776	C&L 2003		0.206	0.742	BGR
	0.38	0.40	This Work		0.18	0.86	Z
B0919+06	0.0228	6.70	KLL	B2020+28	0.11	1.35	S&W
	0.00930	16.4	TML		0.046	3.3	C&L 2003
	0.256	0.597	BGR		0.13	1.2	This Work
	0.21	0.73	Z		0.074	2.07	KLL
	0.19	0.81	S&W		0.0614	2.49	TML
	0.015	10	C&L 2003		0.270	0.566	BGR
	0.12	1.2	This Work		0.23	0.67	S&W
B0950+08	1.04	0.147	KLL	B2110+27	0.0986	1.55	C&L 2003
	77.29	0.001977	TML		0.25	0.60	This Work
	$\gg 9.000$	0.01698	BGR		0.0181	8.43	KLL
	13	0.012	Z		0.0406	3.76	TML
	25	0.0060	S&S		0.24	0.64	Z
	20	0.0076	This Work		0.065	2.3	C&L 2003
B1237+25	0.208	0.735	TML	B2315+21	0.062	2.5	This Work
	1.828	0.08358	BGR		0.00973	15.7	KLL
B2315+21	0.0773	1.98	TML	J1612+2008	0.25	0.61	This Work
	0.17	0.88	Z	J1652+2651	0.0045	34	KLL
	0.124	1.23	C&L 2003	<0.084	>1.8	This Work	
J0051+0423	0.17	0.9	This Work	J1758+3030	0.0022	69	KLL
	0.26	0.59	Z	<0.084	>1.8	This Work	
J0137+1654	0.37	0.42	This Work	J2215+1538	<0.084	>1.8	This Work
	0.023	6.6	This Work	J2227+30	0.21	0.74	This Work
J1313+0931	0.31	0.49	This Work	J2253+1516	0.030	5.0	This Work

**Notes.** The reference keys are as follows:

KLL = A. D. Kuz'min et al. (2007): Observed at 111 MHz and fitted to the scattering tail with a truncated exponential.

TML = J. H. Taylor et al. (1993): Measured a scintillation bandwidth at 1 GHz using a correlation method. In actuality, the  $\tau_s$  value in this paper was measured as a scintillation bandwidth, but only reported as a scattering time. Here, we “deconvert” the reported value back to the original scintillation bandwidth before rescaling.

DLK = M. Daszuta et al. (2013): Observed at 1.7 GHz and fitted a 2D Gaussian to the ACF to determine scintillation bandwidth and timescale.

BGR = N. D. R. Bhat et al. (1998): Observed at 327 MHz and fitted a 2D Gaussian to the ACF to determine scintillation bandwidth and timescale.

Z = V. V. Zakharenko et al. (2013): Observed at 10–30 MHz and fitted to the scattering tail with a boxcar-convolved exponential.

S&W = F. G. Smith & N. C. Wright (1985): Observed at 408 MHz and fitted a 2D Gaussian to the ACF to determine scintillation bandwidth and timescale.

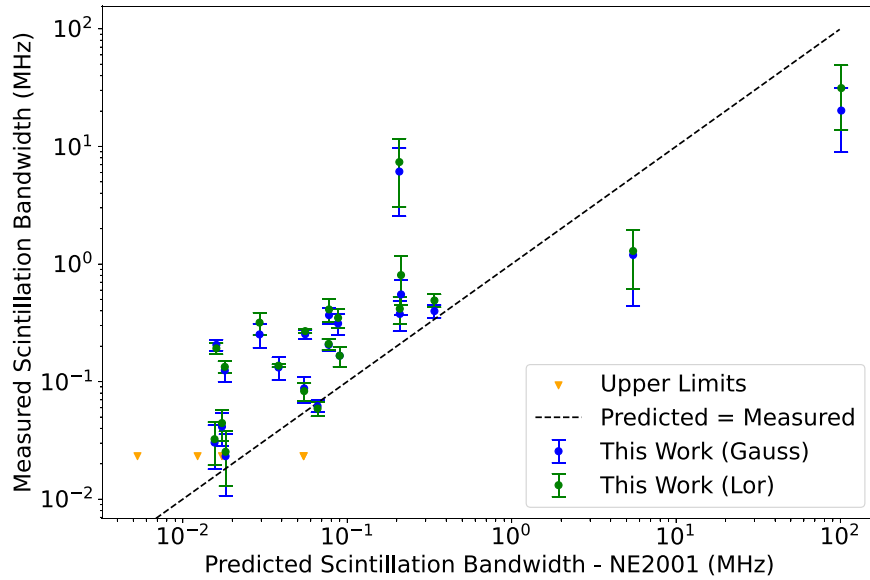
S&S = T. V. Smirnova & V. I. Shishov (2008): Measured a scintillation bandwidth at four frequencies (41, 62, 89, and 112 MHz) using correlation methods. The value we report here is the average.

C&L = J. M. Cordes & T. J. W. Lazio (2003): Compiled scintillation bandwidths from various previous studies; here, all measurements are scintillation bandwidths originally measured in J. Cordes (1986) at 1 GHz using the half-width at half-maximum of the intensity correlation function of the dynamic spectrum.

frequencies. We were only able to find upper limits for J1758+3030 and one of two observations of J2215+1538, but scintillation was still visible in the dynamic spectra. For pulsars

B0919+06, J0137+1654, J1652+2651, J2227+3038, J2253+1516, and the other observation of J2215+1538, we report measured bandwidths despite the fact that these pulsars were





**Figure 3.** Predicted scintillation bandwidths from NE2001 plotted against the measured scintillation bandwidths from this study fitted with Gaussians (blue) and Lorentzians (green). Upper limits are shown with gold triangles. In general, the measurements were larger than their corresponding predictions. The  $1\sigma$  errors are displayed for the measured scintillation bandwidth, as calculated in Section 3.7.

outside the error bars on the NE2001 prediction used to guide sample selection in Section 2.2.

#### 4.5. B0820+02

We made two measurements of B0820+02, which are consistent with each other within  $1\sigma$  error. Both measurements are larger than the model predictions, especially compared to YMW16. J. H. Taylor et al. (1993) was more consistent with the model predictions, while the lower limit from F. G. Smith & N. C. Wright (1985) was an order-of-magnitude larger than the measurements in this work. It should be noted that B0820+02 is in a binary system with a white dwarf companion of mass  $0.6 M_{\text{Sun}}$  (D. Koester & D. Reimers 2000). In the initial folding and assessment with `prepfold`, we observed no significant deviation from vertical in the time-phase plots, indicating that the effect of binarity on the data were minimal. Therefore, we used the simple, non-ephemeris solution when analyzing this pulsar. B0820+02 is also of interest due to its nulling and subpulse drifting behavior (Q. Zhi et al. 2023).

#### 4.6. B0919+06

According to model predictions, we should not have been able to resolve scintles for this pulsar at our observing frequency. However, we obtained three measurements of B0919+06, all an order-of-magnitude larger than predictions from both YMW16 and NE2001, two of which were consistent within error. These measurements were generally larger than A. D. Kuz'min et al. (2007) and J. H. Taylor et al. (1993), but smaller than N. D. R. Bhat et al. (1998), V. V. Zakharenko et al. (2013), and F. G. Smith & N. C. Wright (1985). The mean for the Lorentzian measurement was  $0.13 \pm 0.01$  MHz, and for the Gaussian measurement was  $0.13 \pm 0.02$  MHz.

#### 4.7. B2020+28

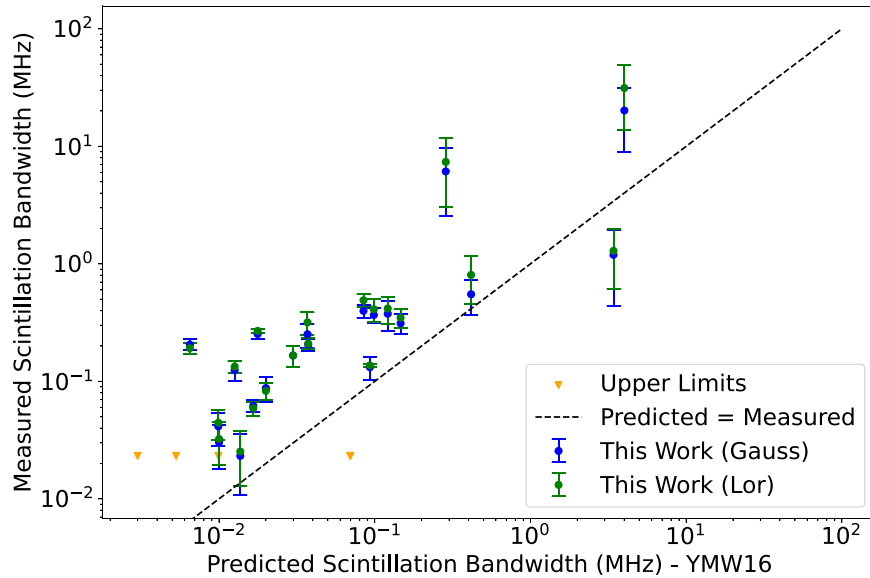
We measured three scintillation bandwidths for B2020+28, two of which were consistent with each other, but not with NE2001 and YMW16 predictions. These measurements were

consistent with F. G. Smith & N. C. Wright (1985), but not J. H. Taylor et al. (1993), N. D. R. Bhat et al. (1998), or A. D. Kuz'min et al. (2007). The mean for the Lorentzian measurement was  $0.27 \pm 0.01$  MHz and for the Gaussian measurement was  $0.25 \pm 0.02$  MHz.

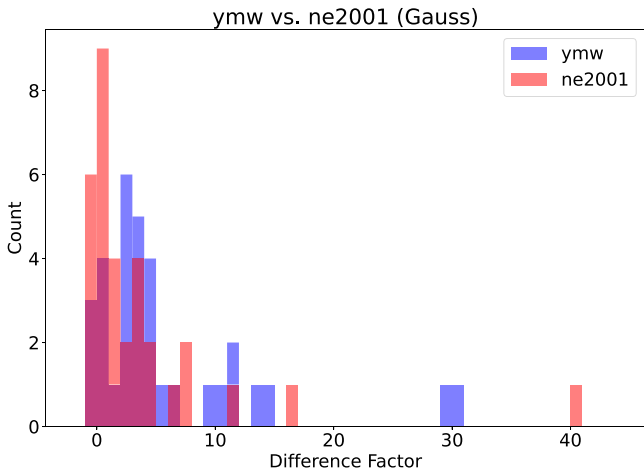
#### 4.8. Population Studies

Our measurements compare to the NE2001 predictions as shown in Figure 3. In almost every case, the measurements that we report in Section 4 are larger than their corresponding NE2001 predictions. A few observations showed clear scintillation in the dynamic spectra, but did not produce a peak in the ACF wider than five points across the profile, implying that there was a scintillation bandwidth but that it was too narrow to resolve with our frequency resolution. These five measurements are indicated in the gold triangles in Figure 3. Note that these are reported with a generous 0.084 MHz upper limit in Table 1; some measured values in other pulsars are narrower than this upper limit due to the difference between the total width across the cropped slice and the extracted width parameter of the fitted function. We do the same analysis for YMW16 predictions in Figure 4 and find an even stronger underprediction than with NE2001.

At this point, it should be noted that the predictions themselves make inherent assumptions about the frequency scaling of scintillation bandwidths and their relation to scattering delays. In this work, both the NE2001 predictions and the YMW16 predictions were obtained by using a Kolmogorov scaling ( $\alpha = 4.4$ ) to shift the predictions from the default value of 1 GHz–327 MHz. NE2001 did use  $\alpha = 4.4$  in the model creation, but YMW16 used the square-law scaling  $\alpha = 4.0$  instead. We also tried an  $\alpha = 4.0$  rescaling of predicted bandwidths for both NE2001 and YMW16, and found hints that the scaling is shallower than 4.4. However, none of the conclusions in the rest of this section are affected by the change in scaling, and it is not consistent to post facto adjust and compare the scalings without going back to the measurements



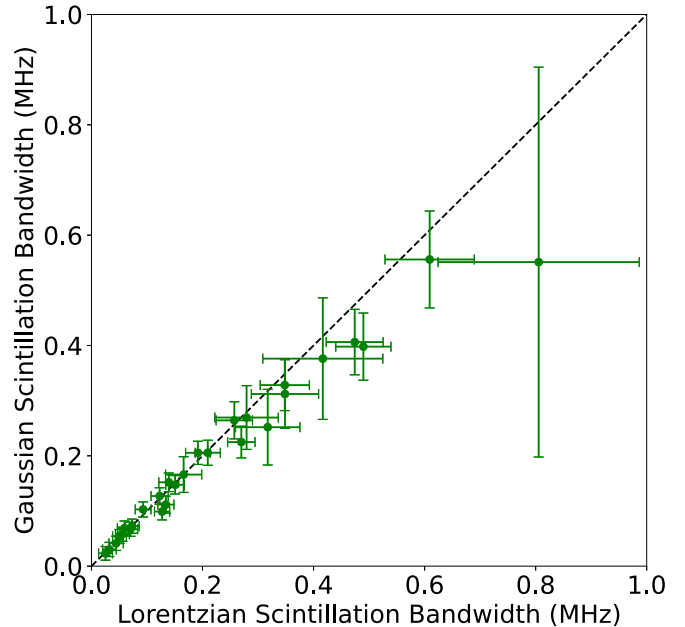
**Figure 4.** Predicted scintillation bandwidths using M. A. Krishnakumar et al. (2015) (YMW16) plotted against the measured scintillation bandwidths from this study fitted with Gaussians (blue) and Lorentzians (green). Upper limits are shown with gold triangles. Even more strongly than with NE2001, the measurements were larger than their corresponding predictions. The  $1\sigma$  errors are displayed for the measured scintillation bandwidth, as calculated in Section 3.7.



**Figure 5.** A histogram comparing the distribution of DF (i.e., the consistency of the model with the data) for YMW16 vs. NE2001 predictions compared to data with Gaussian fits. Even with a small sample size, it is clear that the NE2001 distribution peaks closer to zero than the YMW16 distribution in the left-hand plot, indicating that NE2001 is a better fit to the data.

and observing frequencies that each model is based on and rescaling.

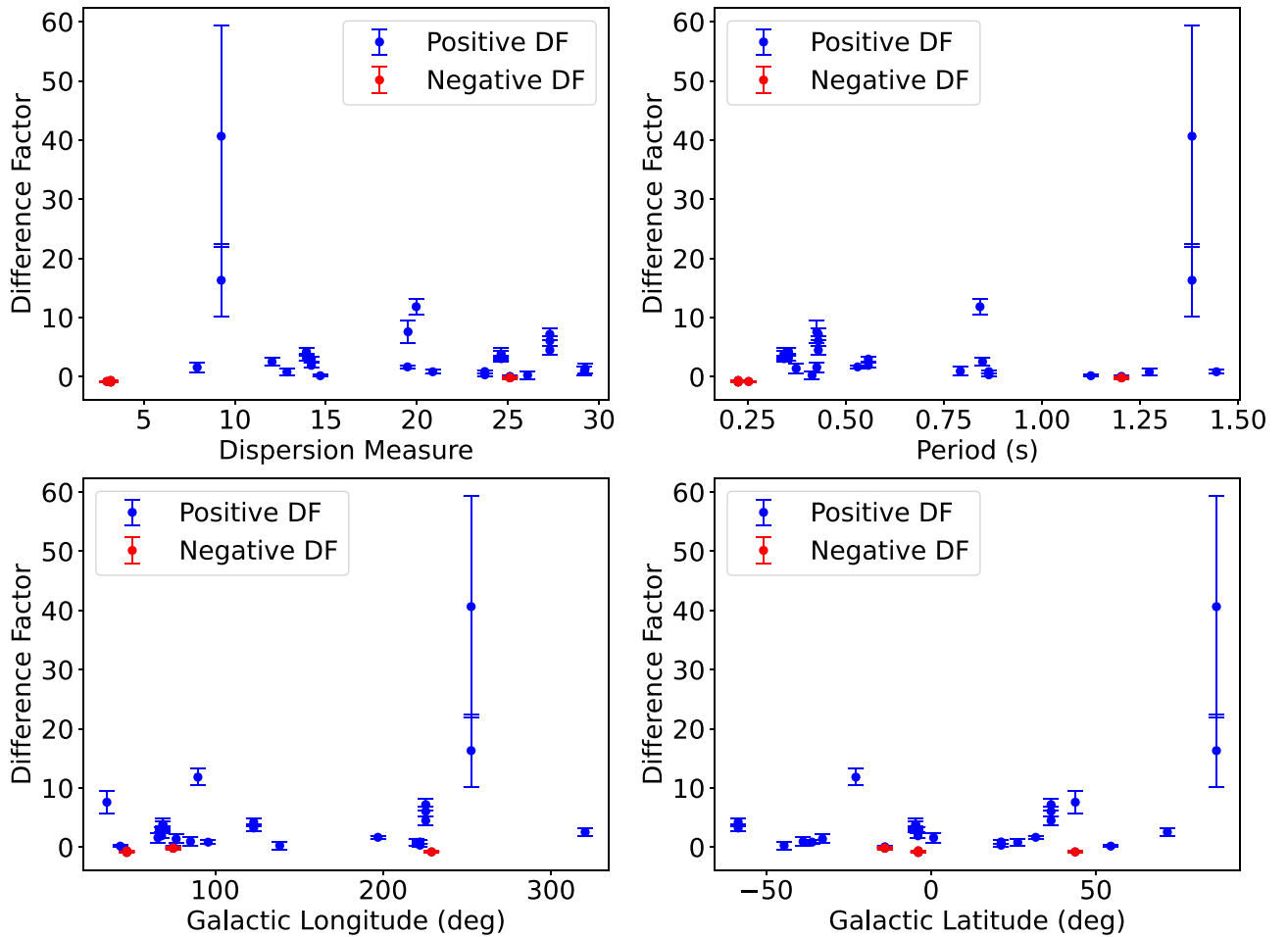
Given that the measurements consistently deviated from the predictions, we evaluated whether these deviations were systematically linked to any physically meaningful parameter. Remember that the DF is dependent upon which model  $\nu_{D,\text{predicted}}$  (NE2001 or YMW16) is being used, as well as which fit function  $\nu_{D,\text{measured}}$  is selected for the reported bandwidth. We found that the combination of model and fit function with the lowest median DF was a Gaussian model fit combined with NE2001 predictions, with a median DF of 1.59. A Lorentzian model fit with YMW16 predictions was the worst of the options, with a median DF of 3.49, while a Gaussian model fit with YMW16 predictions was only slightly better, with a median DF of 3.16. It seems clear that NE2001 is a better match to our data than YMW16 (see Figure 5). The difference between the Gaussian and Lorentzian fits, assuming NE2001, is



**Figure 6.** A scatterplot comparing the Lorentzian (x-axis) and Gaussian (y-axis) scintillation bandwidth measurements below 1 MHz. The Gaussian and Lorentzian measurements for each scintillation bandwidth are generally similar, but the Lorentzians start trending larger at larger scintillation bandwidths (this trend continues into the four measurements above 1 GHz but was omitted for plot readability). The  $1\sigma$  errors are displayed for each fit, as calculated in Section 3.7.

actually quite small; a Lorentzian model fit with NE2001 predictions produces a median DF of 1.72. This is shown graphically in Figure 6, where the Gaussian and Lorentzian measurements are generally similar, except that the Lorentzian measurements trend larger than the Gaussian measurements at larger scintillation bandwidths. A slight preference for the Gaussian fit is expected; previous measurements and models, including NE2001, often made the Gaussian approximation.

In addition, if we divide our sample into pulsars which were used for training NE2001 (as in Table 3 of J. M. Cordes &



**Figure 7.** Correlations between DF (Gaussian fit vs. NE2001) and DM (top left-hand panel), period (top right-hand panel), galactic longitude (bottom left-hand panel), and galactic latitude (bottom right-hand panel). While no universal trends are visible, the presence of measurements with negative DF at low DMs and periods, and the high DF on the pulsar furthest from the galactic plane, could point to differing accuracy of NE2001 in certain directions and distances. The  $1\sigma$  errors are displayed for the DF, calculated using only measurement errors from Section 3.7 (not model errors). The two points with large DF and error bars near  $250^\circ$  galactic longitude belong to B1237+25, whose measured scintillation bandwidths were significantly larger than the prediction when compared to the rest of the sample. Large measured bandwidths are associated with larger absolute errors, which are exaggerated in this case by the small predicted bandwidth.

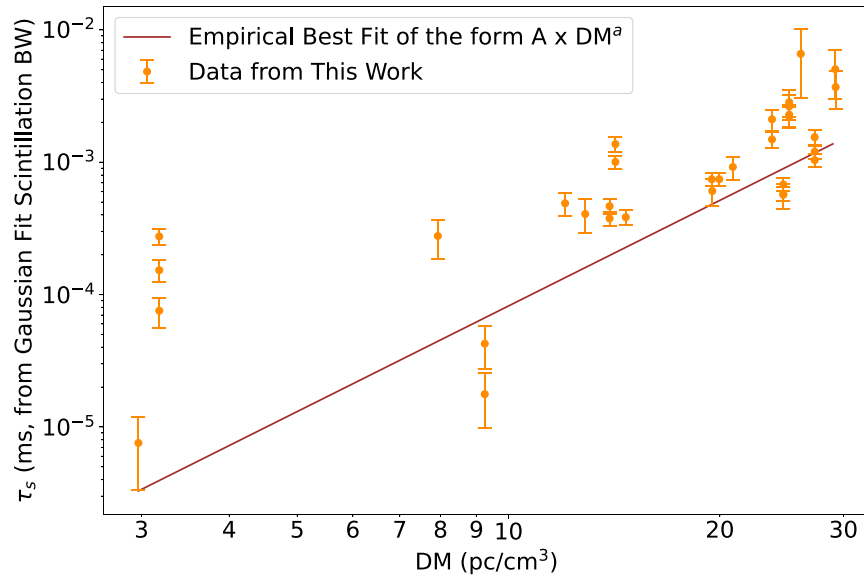
T. J. W. Lazio 2003) and pulsars which were not—conveniently divided along the lines of “B” and “J” labeled pulsars, respectively, in our Table 1—we find that the pulsars that were used for training NE2001 have a median DF of 0.90 (NE2001, Gaussian), as opposed to the pulsars that were not used for training NE2001, which have a median DF of 2.89 (NE2001, Gaussian). We thus confirm that the pulsars that were used for training NE2001 generally conform more closely to the NE2001 model predictions.

Given that the combination of NE2001 and Gaussian has the lowest average DF, we plotted the DF for a Gaussian fit versus NE2001 against the DM, spin period  $P$ , galactic latitude, and galactic longitude for each pulsar, as shown in Figure 7. We also visually inspected all four possible combinations of model and fit function, determining that there is no difference in correlations between any of the four.

Although we do not see any general trends or linear correlations between DF and any of the variables, some interesting conclusions can still be drawn from the rare cases where the prediction exceeded the measurement (shown in red) or where the DF was highest i.e., where the measurement far exceeded the prediction.

From the DM and period subplots, we note that the measurements with negative DF are associated with pulsars that are nearby and have short spin periods. However, only three pulsars show measurements with negative DF, and only two of those, B1929+10 and B0950+08, are driving this conclusion (albeit two pulsars that are in very different parts of the sky). Finally, we note that the pulsar with the largest two measurements of DF, B1237+25, is located extremely far from the galactic plane at a galactic latitude of  $86^\circ.54$ . Given that there are far more galactic radio sources within the galactic plane, it is reasonable that electron density models may be less accurate far from the plane.

Finally, we investigate the possibility of a  $DM-\tau_s$  relation in our data by converting from scintillation bandwidth as in Equation (1), with  $C=0.96$  (Figure 8). Both M. A. Krishnakumar et al. (2015) and J. Cordes et al. (2016) empirically fit their data with a relation of the form  $\tau_s(\text{ms})=A \times DM^a(1+B \times DM^b)$  (as in R. Ramachandran & D. Bhattacharya 1997) where the parenthetical component of the equation (i.e., the steeper positive slope in a log–log plot) becomes dominant for pulsars with DMs greater than a few dozen. In this work, where the largest DM is  $29.24 \text{ pc cm}^{-3}$ , we opt to fit a simpler equation of the form  $\tau_s(\text{ms})=A \times DM^a$



**Figure 8.** DM vs. scattering time in ms, shown on logarithmic axes. The orange points indicate the DM and  $\tau_s$  values from our measurements, while the brown line shows the best fit of the form  $A \times DM^a$ . We find that the DM scaling method somewhat matches our data set, with best-fit parameters of  $A = 2.1 \times 10^{-1}$  and  $a = 2.6$ , but there is still significant scatter. We display  $1\sigma$  errors for the converted scattering time, as calculated in Section 3.7. Note that the sizes of the error bars span four orders-of-magnitude, and points with smaller error bars are significantly upweighted in the fit; this can be difficult to gauge visually given that points with different magnitudes of error bars can look deceptively similar in log-log plotting.

using the `curve_fit` function from `scipy.optimize` with errors incorporated. We find  $A = 1.83 \times 10^{-7}$  and  $a = 2.65$ . J. Cordes et al. (2016) found that  $A = 2.98 \times 10^{-7}$ , and  $a = 1.4$ , while M. A. Krishnakumar et al. (2015) found that  $A = 3.6 \times 10^{-6}$  and  $a = 2.2$ . Our  $A$  value is thus smaller than both previous references, although more consistent with J. Cordes et al. (2016), and our  $a$  value is larger than both previous references, though more consistent with M. A. Krishnakumar et al. (2015). Figure 8 indicates that the DM scaling method can be applied to this data set with some success, but the large residuals indicate that additional effects are likely present.

## 5. Discussion and Conclusion

In this work, we used archival drift-scan data from the Arecibo telescope’s AO327 survey to measure 38 scintillation bandwidths ( $\Delta\nu_D$ ) from 23 pulsars, six of which have no existing  $\Delta\nu_D$  values in the literature. We fit Lorentzian and Gaussian models to the 2D ACFs of the dynamic spectra from these observations, as reported in Section 3, and compared them to the predictions from the NE2001 and YMW16 models of galactic electron density. Generally, in Section 4, we found that our measurements were larger than those predicted by both electron density models. We required at least five points across the profile for the Gaussian and Lorentzian fits, though under-resolution of the profile could still play a role in the general underestimation of the models. We found that NE2001 provided smaller DFs (measuring the difference between the data and the model prediction) than YMW16. We also found that the Gaussian fits were, on average, closer to the model predictions than the Lorentzian fits. While there should be a Fourier relationship between the Lorentzian and the assumed exponential response function of the ISM (J. E. Turner et al. 2024), Gaussians have traditionally been used for fitting throughout the literature, including for NE2001’s training pulsars. The significant presence of NE2001 training pulsars in

this data set thus potentially explains the success of the Gaussian fit.

Using Gaussian fits, we found that the scintillation bandwidths measured for three nearby millisecond pulsars were smaller than NE2001 predictions, breaking the trend set by the other 20 pulsars (see Section 4.2). In addition, four pulsars showed scintillation that was too narrow to measure (reported as an upper limit; see Section 4.3). We see no general trend with DF (Gaussian fit, NE2001) versus DM, period, or galactic coordinates, but do see some indication that NE2001 is less accurate far from the galactic plane and at low distances from Earth (Section 4.8).

At a high level, there is a question of whether direction-agnostic DM scaling approaches (e.g., M. A. Krishnakumar et al. 2015) or the modeling of large-scale distribution of interstellar scattering (e.g., J. M. Cordes & T. J. W. Lazio 2002) more successfully predict scintillation bandwidths. Here, despite the challenges of modeling electron density geometrically, NE2001 produces a better fit to the data i.e., smaller DFs. These measurements could be used to inform the distribution of interstellar scattering and turbulence properties in the next generation of geometric models.

In Section 4, specifically the literature review in Table 2, we also find that previous  $\Delta\nu_D$  values for these pulsars in the literature are generally in agreement with each other and with our measurements in order-of-magnitude, but often disagree by factors of a few, barring some egregious outliers. Some of the disagreement could be due to the assumption of a Kolmogorov scaling of  $\alpha = 4.4$ , which was used to make various sources compatible. More of it is likely due to true changes in the scintillation bandwidth over the years and decades between references given that scintillation bandwidths can change dramatically even over months-long timescales (e.g., D. A. Hemberger & D. R. Stinebring 2008). Even so, for pulsars that had three or more measurements in our sample, we do not see any indication that observations taken closer together in time have better agreement in their scintillation





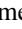

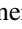
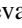
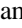
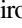
bandwidth measurements than observations taken far apart. To better investigate this phenomenon, future work could more thoroughly account for DM changes over time, as discussed in B. J. Shapiro-Albert et al. (2021).

This work covers about 97% of the PUPPI data from the AO327 project, which were searched for a subset of 40% of the pulsars in the J. S. Deneva et al. (2024) sample. With the pipeline described in Section 3 fully implemented, this pilot survey can be expanded to the full set of AO327 pulsar detections, including the earlier data taken with the Mock Spectrometer, providing a uniform sample against which to compare future  $\Delta\nu_D$  measurements in the literature. This is increasingly relevant due to the connections between better pulsar timing and the detection and characterization of low-frequency gravitational waves.

### Acknowledgments

S.Z.S. acknowledges that this material is based upon work supported by the National Science Foundation MPS-Ascend Postdoctoral Research Fellowship under grant No. 2138147. This work was performed as part of the Penn State Pulsar Search Collaboratory, which is an offshoot of the Pulsar Search Collaboratory project funded under NSF award No. 151651. This project used archival data from the AO327 project, funded under NSF award No. 2009425, and utilized resources from the NANOGrav Physics Frontiers Center, funded under NSF award No. 2020265. M.T.L. acknowledges support received from NSF AAG award No. 2009468, and NSF Physics Frontiers Center award No. 2020265, which supports the NANOGrav project. M.A.M. is supported by NSF Physics Frontiers Center award No. 2020265 and NSF award No. 2009425. Figure 1 was created using the SankeyMATIC software (<https://github.com/nowthis/sankeymatic>).

### ORCID iDs

Sofia Sheikh  <https://orcid.org/0000-0001-7057-4999>  
 Grayce C. Brown  <https://orcid.org/0000-0002-0069-2778>  
 Jackson MacTaggart  <https://orcid.org/0000-0002-4753-4638>  
 Thomas Nguyen  <https://orcid.org/0000-0002-4949-9821>  
 Vincent A. Smedile  <https://orcid.org/0009-0008-8819-0481>  
 Maura A. McLaughlin  <https://orcid.org/0000-0001-7697-7422>  
 Jacob E. Turner  <https://orcid.org/0000-0002-2451-7288>  
 Julia S. Deneva  <https://orcid.org/0000-0003-1226-0793>  
 Michael T. Lam  <https://orcid.org/0000-0003-0721-651X>  
 Brent J. Shapiro-Albert  <https://orcid.org/0000-0002-7283-1124>

### References

Agazie, G., Alam, M. F., Anumlapudi, A., et al. 2023, *ApJL*, 951, L9  
 Arzoumanian, Z., Baker, P. T., Blecha, L., et al. 2023, *ApJL*, 951, L28  
 Bhat, N. D. R., Gupta, Y., & Rao, A. P. 1998, *ApJ*, 500, 262  
 Bogart, S., 2024 SankeyMATIC, v1.2.0, <https://sankeymatic.com/>

Chen, S., Caballero, R. N., Guo, Y. J., et al. 2021, *MNRAS*, 508, 4970  
 Cordes, J. 1986, *ApJ*, 311, 183  
 Cordes, J., & Shannon, R. 2010, arXiv:1010.3785  
 Cordes, J., Wharton, R., Spitler, L., Chatterjee, S., & Wasserman, I. 2016, arXiv:1605.05890  
 Cordes, J. M., & Lazio, T. J. W. 2002, arXiv:astro-ph/0207156  
 Cordes, J. M., & Lazio, T. J. W. 2003, arXiv:astro-ph/0301598  
 Cordes, J. M., & Rickett, B. J. 1998, *ApJ*, 507, 846  
 Cordes, J. M., Rickett, B. J., Stinebring, D. R., & Coles, W. A. 2006, *ApJ*, 637, 346  
 Daszuta, M., Lewandowski, W., & Kijak, J. 2013, *MNRAS*, 436, 2492  
 Deller, A. T., Goss, W. M., Brisken, W. F., et al. 2019, *ApJ*, 875, 100  
 Deneva, J. S., McLaughlin, M., Olszanski, T. E. E., et al. 2024, *ApJS*, 271, 23  
 Deneva, J. S., Stovall, K., McLaughlin, M. A., et al. 2013, *ApJ*, 775, 51  
 Deneva, J. S., Stovall, K., McLaughlin, M. A., et al. 2016, *ApJ*, 821, 10  
 Ferguson, D. C., Perillat, P., & Vayner, B. 2022, *JanSc*, 69, 139  
 Hemberger, D. A., & Stinebring, D. R. 2008, *ApJL*, 674, L37  
 Hewish, A., Bell, S. J., Pilkington, J. D. H., Scott, P. F., & Collins, R. A. 1968, *Natur*, 217, 709  
 Hotan, A. W., van Straten, W., & Manchester, R. N. 2004, *PASA*, 21, 302  
 Jow, D. L., Pen, U.-L., & Feldbrugge, J. 2023, *MNRAS*, 525, 2107  
 Koester, D., & Reimers, D. 2000, *A&A*, 364, L66  
 Krishnakumar, M. A., Mitra, D., Naidu, A., Joshi, B. C., & Manoharan, P. K. 2015, *ApJ*, 804, 23  
 Kuz'min, A. D., Losovskii, B. Y., & Lapaev, K. A. 2007, *ARep*, 51, 615  
 Lam, M., 2017 PyPulse: PSRFITS handler, Astrophysics Source Code Library, ascl:1706.011  
 Levin, L., McLaughlin, M. A., Jones, G., et al. 2016, *ApJ*, 818, 166  
 Liu, Y., Verbiest, J. P. W., Main, R. A., et al. 2022, *A&A*, 664, A116  
 Lorimer, D. R. 2008, *LRR*, 11, 1  
 Manchester, R. N., Hobbs, G. B., Teoh, A., & Hobbs, M. 2005, *AJ*, 129, 1993  
 Martinez, J. G., Gentile, P., Freire, P. C. C., et al. 2019, *ApJ*, 881, 166  
 Ocker, S. K., Cordes, J. M., & Chatterjee, S. 2020, *ApJ*, 897, 124  
 Price, D. C., Flynn, C., & Deller, A. 2021, *PASA*, 38, e038  
 Ramachandran, R., & Bhattacharya, D. 1997, *MNRAS*, 288, 565  
 Ransom, S., 2011 PRESTO: Pulsar Exploration and Search Toolkit, Astrophysics Source Code Library, ascl:1107.017  
 Reardon, D. J., Coles, W. A., Bailes, M., et al. 2020, *ApJ*, 904, 104  
 Reardon, D. J., Shannon, R. M., Cameron, A. D., et al. 2021, *MNRAS*, 507, 2137  
 Rickett, B. J. 1977, *ARA&A*, 15, 479  
 Rickett, B. J. 1990, *ARA&A*, 28, 561  
 Rickett, B. J., & Lyne, A. G. 1990, *MNRAS*, 244, 68  
 Ruderman, M. 1972, *ARA&A*, 10, 427  
 Shapiro-Albert, B. J., Hazboun, J. S., McLaughlin, M. A., & Lam, M. T. 2021, *ApJ*, 909, 219  
 Smirnova, T. V., & Shishov, V. I. 2008, *ARep*, 52, 736  
 Smith, F. G., & Wright, N. C. 1985, *MNRAS*, 214, 97  
 Stinebring, D. R., McLaughlin, M. A., Cordes, J. M., et al. 2001, *ApJL*, 549, L97  
 Tarafdar, P., Nobleson, K., Rana, P., et al. 2022, *PASA*, 39, e053  
 Taylor, J. H., Manchester, R. N., & Lyne, A. G. 1993, *ApJS*, 88, 529  
 Turner, J. E., Joshi, B. C., McLaughlin, M. A., & Stinebring, D. R. 2024, *ApJ*, 961, 101  
 Turner, J. E., McLaughlin, M. A., Cordes, J. M., et al. 2021, *ApJ*, 917, 10  
 Virtanen, P., Gommers, R., Oliphant, T. E., et al. 2020, *NatMe*, 17, 261  
 Walker, M. A., Melrose, D. B., Stinebring, D. R., & Zhang, C. M. 2004, *MNRAS*, 354, 43  
 Wang, N., Manchester, R. N., Johnston, S., et al. 2005, *MNRAS*, 358, 270  
 Wu, Z., Verbiest, J. P. W., Main, R. A., et al. 2022, *A&A*, 663, A116  
 Yao, J. M., Manchester, R. N., & Wang, N. 2017, *ApJ*, 835, 29  
 Zakharenko, V. V., Vasylieva, I. Y., Konvalenko, A. A., et al. 2013, *MNRAS*, 431, 3624  
 Zhi, Q., Xu, X., Shang, L., et al. 2023, *MNRAS*, 520, 1332